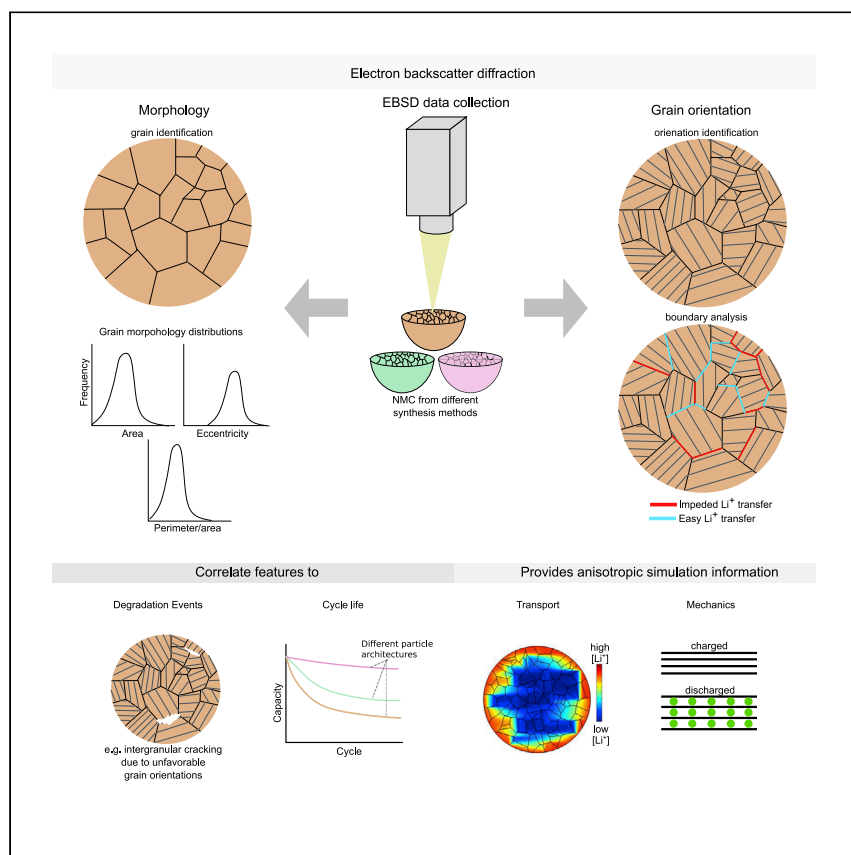Article

Electron Backscatter Diffraction for Investigating Lithium-Ion Electrode Particle Architectures

Alexander Quinn, Helio Moutinho, Francois Usseglio-Viretta, Ankit Verma, Kandler Smith, Matthew Keyser, Donal P. Finegan

donal.finegan@nrel.gov

HIGHLIGHTS

Grain orientation and boundaries in battery electrode materials are understudied

EBSD provides ample orientation, boundary, and morphology information

Potential effects on degradation and cycling because of grain orientation are discussed

EBSD should be extended to 3D to get complete orientation and morphology information

Battery lifetime and performance could be improved by tuning electrode particle crystal orientation, grain boundary, and morphology features. Quinn et al. show that electron backscatter diffraction provides these features and discuss its implications for degradation and charge time. The technique is extensible to 3D and can inform new anisotropic simulations.

Article

Electron Backscatter Diffraction for Investigating Lithium-Ion Electrode Particle Architectures

Alexander Quinn,[1] Helio Moutinho,[2] Francois Usseglio-Viretta,[1] Ankit Verma,[1] Kandler Smith,[1] Matthew Keyser,[1] and Donal P. Finegan[1,3,*]

SUMMARY

The performance and degradation of layered cathode materials for lithium-ion batteries depend on their morphological, surface, and crystallographic properties. A comprehensive tool to spatially characterize grain geometry and orientation in electrode particles is needed in order to understand solid-state lithium transport and the efficacy of particles to avoid lithiation heterogeneities and strain-induced degradation. Here we apply electron backscatter diffraction on $LiNi_{0.5}Mn_{0.3}Co_{0.2}O_2$ particle cross-sections to spatially describe intra-particle grain architectures. A method for segmenting, labeling, and quantifying morphological properties of distinct grains is developed and applied. Crystallographic orientations are measured for each grain, and the spatial distribution of grain orientations is quantified with a specific focus on describing lithium transport and accounting for inter-grain lithiation barriers. The necessary extension from two-dimensional to three-dimensional descriptions of grain morphologies and orientations to predict lithiation inefficiencies is discussed, as well as a method to quantify the ideality of grain architectures for high-rate and efficient operation.

INTRODUCTION

The most common lithium-ion (Li^+) battery cathode materials are intercalation electrodes, which reversibly store Li^+ without major crystal structure changes because of the redox reactions. Intercalation cathode materials are subdivided according to the crystal structure; for instance, layered, spinel, olivine, and tavorite.[1] Most cathode materials used in Li^+ batteries today consist of layered structures, where Li^+ primarily transport through the crystal along two-dimensional (2D) planes. The most common layered cathode is $LiNi_xMn_yCo_zO_2$ (NMC), which is mostly synthesized to form polycrystalline particles with differently sized and oriented crystals.[2] We clarify the nomenclature used here for the polycrystalline structure. Particle refers to the largest NMC unit, a roughly spherical agglomerate of grains. A grain can be a single crystallite or contain multiple crystallites. A crystallite is the most basic NMC unit, an atomically ordered and layered material with a specific and uniform orientation. Elsewhere, grains might be referred to as "primary particles" or refer to the definition of a crystallite. In the bulk of the electrode, heterogeneities in state of charge and degradation partially occur because of the pore structure hindering ionic transport, resulting in variable availability of Li^+ to particles along the electrode thickness.[3–8] Similar limitations occur at the sub-particle level, where the grains of varied orientation only allow Li^+ to travel along specific crystal planes,[9] and the dynamics of the

[1]Center for Integrated Mobility Sciences, National Renewable Energy Laboratory, 15013 Denver W. Pkwy., Golden, CO 80401, USA

[2]Materials Science, National Renewable Energy Laboratory, 15013 Denver W. Pkwy., Golden, CO 80401, USA

[3]Lead Contact

*Correspondence: donal.finegan@nrel.gov

https://doi.org/10.1016/j.xcrp.2020.100137

system are governed by solid-state Li^+ transport, which depends strongly on the state of charge.[10,11] Thus, with a distribution of grain morphologies and orientations within a particle, Li^+ transport is not strictly radially inward (as assumed by the well-established Newman model[12]) but may travel along unfavorable circuitous paths, effectively exhibiting a sub-particle tortuosity.

Evidently, grain orientation, structure, and boundaries control certain degradation modes. Both inter- and intra-granular degradation occur,[13–17] for which multiple mechanisms have been proposed. Intra-granular cracking originates at grain defects and propagates along specific crystallographic planes.[13,14] Inter-granular cracking and void creation is especially prevalent in NMC with high Ni content, which suffers from severe mechanical strain.[16–19] The increased presence of grain boundaries exacerbates heterogeneous degradation, such as through oxygen loss and undesired crystal phase transitions.[20] Layered crystals within polycrystalline transition metal oxides, such as NMC, expand anisotropically[17,21] because of the layered material structure and concentration gradients from inhomogeneous lithiation.[22] The expansion continually disintegrates particles during cycling, resulting in voids and cracks leading to electrical disconnections (thus, an effective loss of active material) and an increase in particle surface area that consumes electrolyte and lithium through growth of the cathode electrolyte interphase.[18,19,23–25] The polycrystalline architecture can either alleviate or promote expansion-induced strains.[19] Surface reconstruction (structural and compositional transformations at crystal surfaces) preferentially spreads along specific crystal facets,[26] which affects local electrochemical and transport characteristics and contributes to mechanical stresses.[26,27] Local crystal phase transformations can also occur within particles, incurring transition metal dissolution and an effective active material loss.[28] Achieving a clear understanding of these processes is complicated by interconnected mechanical, thermal, and chemical mechanisms that alter the state of the intercalation host and affect Li^+ and electron transport.[27,29–32]

Interfaces are also important considerations for polycrystalline material behavior. Many studies have focused on the reactive electrolyte-electrode interface,[32–38] which contributes to degradation.[39,40] An important element of crystal interfaces is that the exposed facet determines the behavior. Specific facets promote intercalation, whereas others prohibit it,[41–44] and certain facets are more unstable than others.[45] Grain boundaries have received relatively little attention but likely have orientation-dependent characteristics. The structure and composition of grain boundary regions remain uncertain. Grain boundary regions might consist of gas pockets; amorphous material;[46] compositions different from the bulk crystal;[26] electrolyte, or its residue;[47] or simply change the crystallographic direction without disorder at the interface.[48] Density functional theory (DFT) studies of transport at boundaries with maintained atomic connectivity demonstrated that energetically favored grain boundary structures slowed Li^+ transport across the boundary compared with the bulk.[49,50] This conclusion may not be universal to all boundaries, though, because DFT studies assume specific atomic configurations at the boundary. The energetically favorable boundary structures might only represent a fraction of boundary configurations found in real polycrystalline particles. Other kinetically trapped boundary structures, which are expected to depend on grain orientations, may have vastly different effects. Transport might be quicker along or near the boundary, potentially circumventing the tortuous paths through poorly aligned grains. Other boundaries might bottleneck transport. To our knowledge, no experiments have probed transport specifically in boundary regions. Classifying interface

types and their distributions may help in understanding cross-boundary transport and their role in degradation.

Although a plethora of spatial information has been gathered on NMC materials, most current studies ignore crystal orientation. Potentially, by synthesizing polycrystals with specific orientations and interfaces, mechanical disintegration could be alleviated, chemical behavior controlled, and impedance to lithiation reduced. Specifically correlating void and crack origination with grain orientation and morphology descriptions could lead to identification of particle architectures prone to degradation. Commercially relevant NMC particles, especially under fast charging, operate in a diffusion-limited regime, suggesting the importance of understanding sub-particle transport.[51] A quick method to evaluate grain orientations and interfaces is desired to study the variants in polycrystalline and chemical configurations of electrode materials under various operating conditions. For example, operating conditions such as charging at high voltage[13,52] or high current[53–55] aggravate degradation, and under varying operating conditions, different degradation modes predominate.

Electron backscatter diffraction (EBSD) is a promising technique for acquiring grain orientations and boundaries.[56] EBSD spatially resolves the orientation of identified grains, quantifies the confidence of orientation assignments, and can provide limited grain boundary information.[57] EBSD is suitable for widespread use because of common integration of EBSD detectors into scanning electron microscopy (SEM) instruments and can be extended to three-dimensional (3D) to capture full particle architectures through serial milling with a focused ion beam (FIB). EBSD typical image resolution is 20–50 nm with an angular resolution of 0.5°, and the scan area is limited by the minimum magnification of the SEM, allowing detailed characterization of single electrode particles.

Here we describe a method for quantifying polycrystalline NMC architectures with EBSD. From cross-sectioned particles, EBSD image quality (IQ) maps, which quantify the sharpness of the electron beam diffraction pattern, are used to segment grains within the particles. Two grain boundary types are found: those occupying the low-IQ boundary region produced by the segmentation (inter-grain) and those identified only by misorientation (intra-grain). Grain morphology is described by the area, perimeter, and eccentricity extracted from the processed segmentation. Two metrics are conceived to describe Li^+ transport paths: (1) the orientation of grains to the general lithiation radial direction (noted radial orientation [r-orientation]) and (2) the relative orientation of adjacent grains (noted grain misorientation [g-misorientation]). 3D EBSD analysis using analogous morphology metrics (volume, specific surface area, and sphericity), r-orientation, g-misorientation, and boundary plane orientation should be performed to fully quantify architectures for purposes of simulating heterogeneous transport, mechanics, and other physics.

RESULTS AND DISCUSSION

A Quantification Method for Layered Electrodes

SEM in conjunction with EBSD is a powerful combined tool for quantifying grain orientations and morphologies, such as in NMC. In Figure 1A, an EBSD inverse pole figure (IPF) map presents crystallographic orientations of grains, in the grain reference system, within an entire cross-section of a typical NMC particle, which contains smaller grains. We define grains and particles here using the IQ map in Figure 1B and use the SEM image in Figure 1C as partial validation of the grain boundary locations.
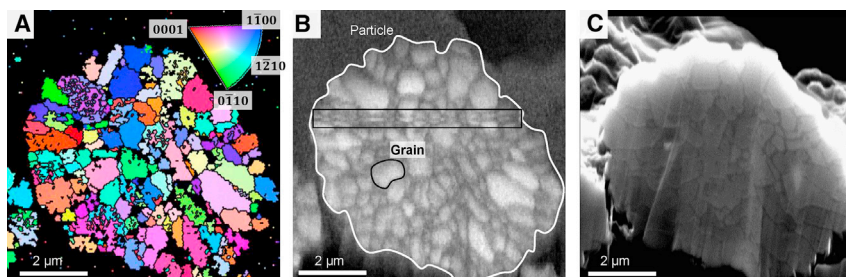
Figure 1. Particle Cross-Sections

(A–C) EBSD IPF map of polycrystalline NMC532 (A), the corresponding EBSD IQ map (B) from which particles and grains were segmented, and a SEM image (C). The boxed region in (B) is an artifact.

In Figure 1A, each color represents a specific direction in the crystal, given as a Miller-Bravais index. Similar colors are alike in orientation. A grain with a specific color has that vector oriented normal to the sample (pointing out of the page). For example, an index of 0001 (red) indicates that the *c* axis of the grain points outward from the page. The $1\bar{1}00$, $0\bar{1}10$, and $1\bar{2}10$ crystal orientations lie on the basal plane and are shown in Figure 2A. Use of the directions 0001, $1\bar{1}00$, $0\bar{1}10$, and $1\bar{2}10$ to describe the orientation space assumes that an equivalent crystal structure is found by rotating the crystal in increments of 60° (6-fold symmetry). The hexagonal unit cell description of NMC contains a trigonal system, meaning that rotation of the unit cell about the *c* axis (0001) produces equivalent structures every 120° (3-fold symmetry), not every 60°. Thus, in certain cases, similar colors in Figure 1A might be different orientations. In addition, the IPF map incompletely describes the 3D orientation of a crystal. IPF maps therefore limit our understanding of NMC orientation. For this reason, we later introduce Bunge-Euler angles and vector-based descriptions.

Processed EBSD data typically include two measures of data quality: IQ and confidence index. A low confidence index (black in Figure 1A) means that the software cannot discern between multiple orientations.[58] Important to these studies is the IQ map in Figure 1B, which is a measure of the quality of the Kikuchi diffraction pattern used to index the crystal orientation. Generally, brighter IQ values indicate a sharper Kikuchi pattern. The IQ value decreases with increasing defects in a grain and higher stresses. Relatively low IQ can also suggest boundary locations because of overlapping crystal signatures.[59] Poor surface preparation or poor crystallinity of the sample results in low IQ, which reduces its usefulness for distinguishing grains. Grains in the SEM image of the same particle (Figure 1C) were low contrast and prohibited clear identification of grains, which readily appear in the EBSD IPF and IQ maps. However, the boundaries in the SEM image are generally sharper, providing finer morphological detail. Grains are often single crystals but, as explored later, can contain multiple crystallites. The processing or detector artifact in the boxed region of the IQ map (Figure 1B) artificially creates boundaries. Our conclusions were not affected here, but boundaries should be verified using multiple techniques.

Figure 1A qualitatively colors alike orientations but with the drawback of information loss because of representing the orientation of a 3D body (the crystal) using only one crystal direction. EBSD provides more complete information: the 3D crystal orientation at each pixel, which is often reported as 3 angles specifying 3 sequential rotations about different axes. To visualize the 3D representation, we use a hexagon to represent the hexagonal structure of an NMC crystal (Figure 2A). The crystal axes *a*, *b*, and *c* are nested into a coordinate system of orthogonal axes *x'*, *y'*, and
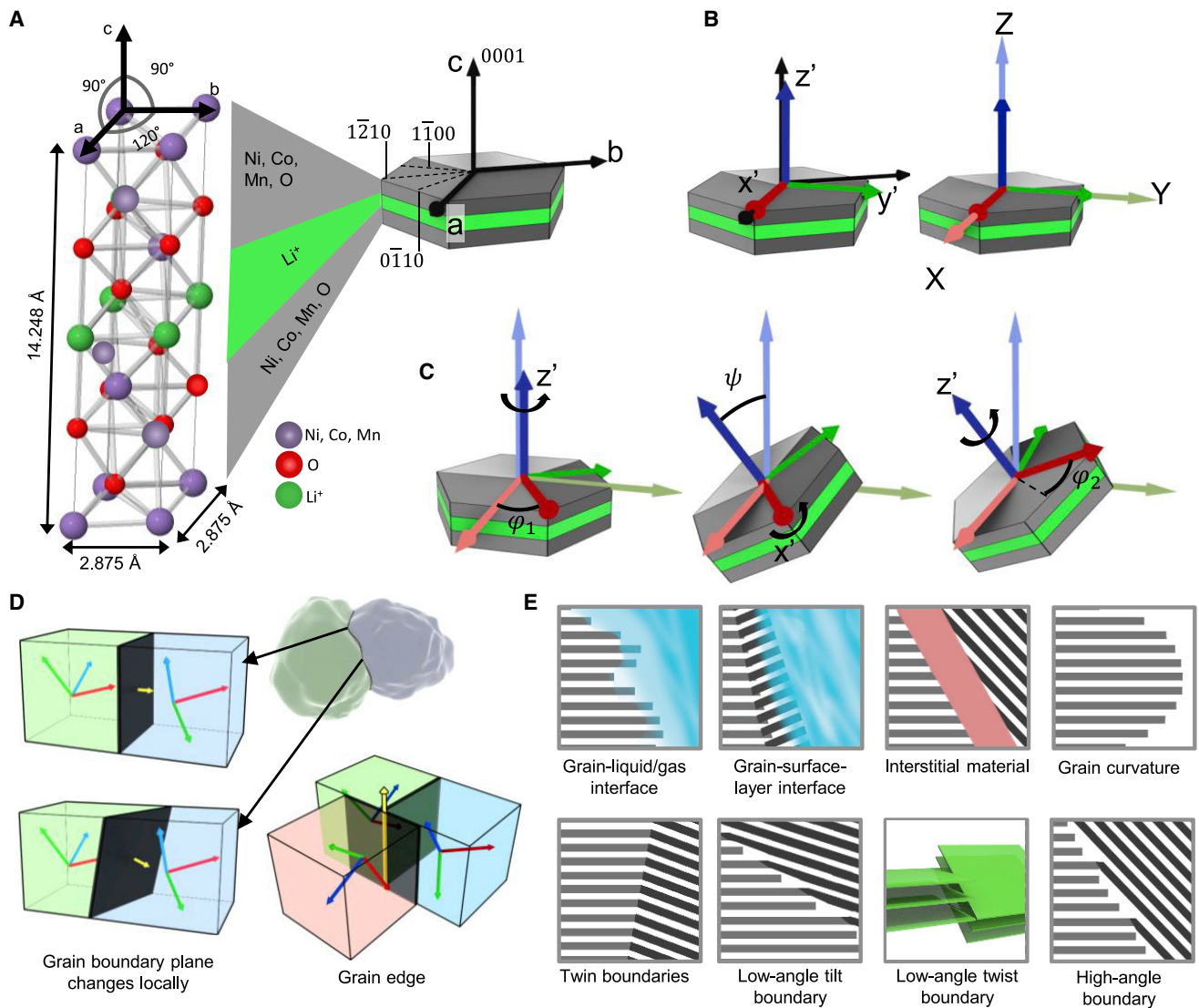
Figure 2. Grain Orientation and Boundary Features

(A) Crystal structure and its simplified representation in hexagonal form. *a*, *b*, and *c* are the crystal axes. Crystal structure parameters were obtained from Ge et. al.[62] and displayed using the Inorganic Crystal Structure Database.[63] Red, green, and purple represent oxygen, Li$^+$, and transition metals (Mn, Co, and Ni), respectively. Various representations exist for the crystal structure (Figure S1).[64,65]

(B) The *x′*, *y′*, and *z′* axes replace the crystal axes *a*, *b*, and *c*. The *x′*, *y′*, and *z′* axes in coincidence with sample axes *X*, *Y*, and *Z* represent the crystal prior to rotation. The sample axes are static; *Z* always points normal to the sample surface.

(C) Three subsequent rotations about the *z′*, *x′*, *z′* crystal axes according to the Bunge-Euler convention describe the grain orientation.

(D) The local boundary plane (black plane) changes orientation along the boundary surface, but the relative orientations of two adjacent grains do not (boxed red, green, and blue regions). Boundary edges (or triple junctions), where two boundary surfaces meet, are shown as an example of a higher-order interface using a yellow arrow that follows the intersection.

(E) Pictorials of various grain boundary features.

z′ (Figure 2B). These 3D coordinates can then be conveniently rotated with respect to a reference frame where, prior to rotation, the *X*, *Y*, and *Z* axes of the reference frame are in coincidence with the respective *x′*, *y′*, and *z′* axes of the crystal frame (Figure 2B). The axes of rotations are a matter of convention. In crystallography, the Bunge-Euler convention is often used, in which rotations are performed in succession about the *z′*, *x′*, and *z′* crystal frame axes with the respective angles φ_1, ψ, and φ_2 (Figure 2C).[60] Equation 1 describes the rotation of any vector [*x y z*]^T to its

new direction $[x_{rot}, y_{rot}, z_{rot}]^T$ because of crystal rotation. For example, $[x\ y\ z]^T$ might point between two atoms in the NMC crystal. Equation 2 is how the rotation matrix, R, is constructed with the Bunge-Euler angles. R contains all necessary information for the bulk orientation of a crystal.
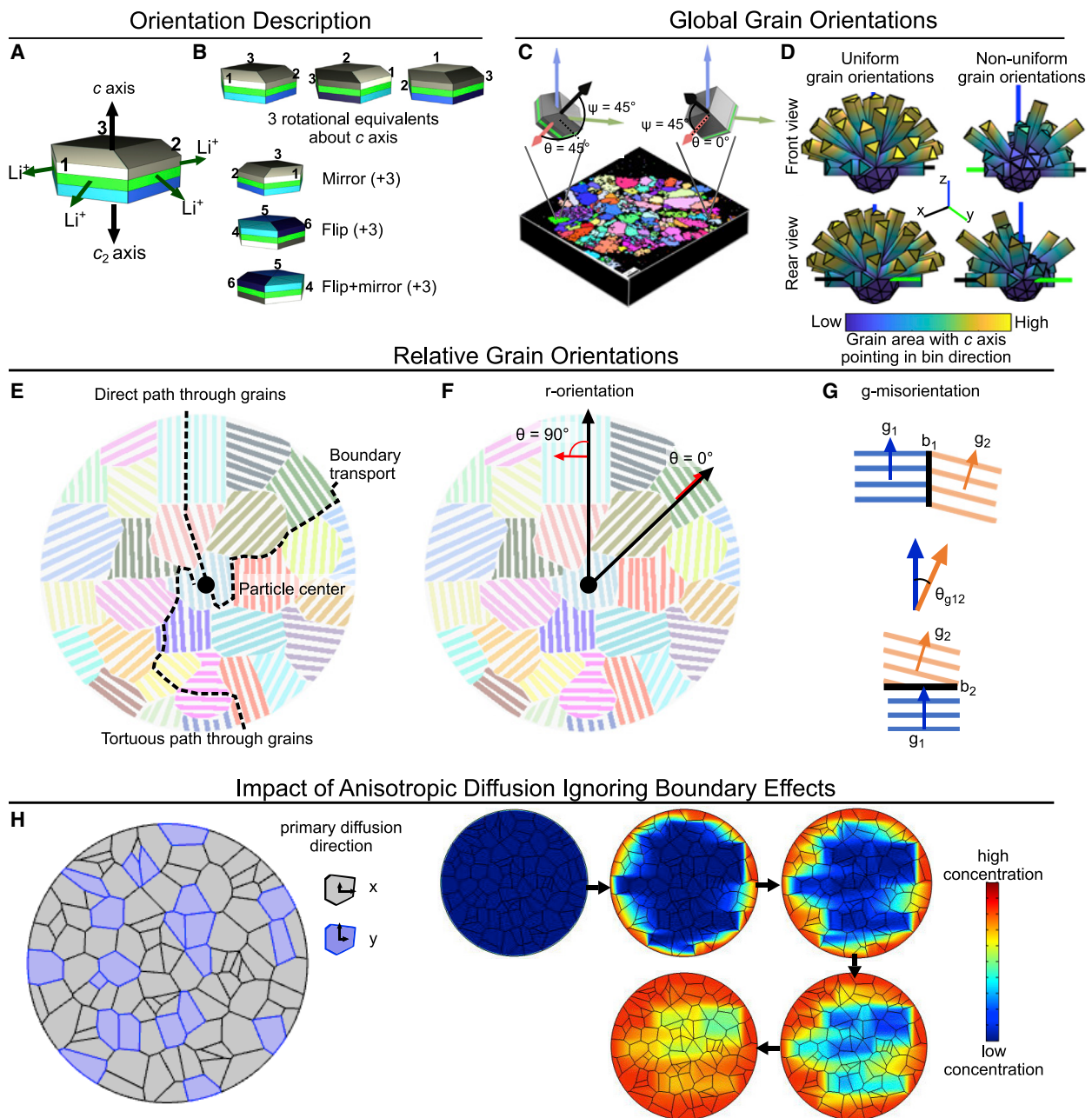
$$R \begin{bmatrix} x \\ y \\ z \end{bmatrix} = \begin{bmatrix} x_{rot} \\ y_{rot} \\ z_{rot} \end{bmatrix} \qquad \text{(Equation 1)}$$

$$R = \begin{bmatrix} \cos\varphi_1 & \sin\varphi_1 & 0 \\ -\sin\varphi_1 & \cos\varphi_1 & 0 \\ 0 & 0 & 1 \end{bmatrix} \begin{bmatrix} 1 & 0 & 0 \\ 0 & \cos\psi & \sin\psi \\ 0 & -\sin\psi & \cos\psi \end{bmatrix} \begin{bmatrix} \cos\varphi_2 & \sin\varphi_2 & 0 \\ -\sin\varphi_2 & \cos\varphi_2 & 0 \\ 0 & 0 & 1 \end{bmatrix}$$

$$\text{(Equation 2)}$$

An analysis applicable to the spherical NMC cathode particles considers relative orientations of adjacent grains for understanding grain-to-grain Li⁺ transport and relative orientations of grains to the particle center, the general direction in which Li⁺ travels during lithiation of the particle. Figure 2D illustrates that grain boundaries are affected by particle morphology and relative grain orientations. To fully describe the boundary between two grains, a minimum of five parameters are needed: three specify the orientation of the grain relative to its neighbor (e.g., with Bunge-Euler angles), and two specify the local orientation of the boundary plane (e.g., the vector of the normal to the boundary plane using spherical coordinates). As an observer moves along the surface of a boundary between 2 grains, the orientation of the plane between the two grains changes whereas the relative orientations of the two grains does not. Higher-order interfaces also exist. Intersecting grain boundaries produce grain edges, which, in 2D cross-sections (such as in Figure 1), are points shared between three grains and are known as triple junctions. Last, points exist where grain edges meet. In decreasing order of volumetric occupancy are the bulk of the grain, grain boundaries, grain edges, and the points at which grain edges intersect. Higher-order interfaces occupy less volume but may still be important because they are structurally less well defined. With 2D EBSD data, it is impossible to extract the direction of the grain boundary plane or higher-order features. Relative orientations of neighboring grains, though, can be calculated and reported with matrix notation[60] or angle-axis pairs.[61] 3D morphology information could allow extraction of boundary topology to complete the boundary description.

Grain boundaries might manifest in multiple ways, including in combinations of features, as pictured in Figure 2E. The examples shown serve to highlight that boundary structure might vary throughout a single polycrystalline NMC particle, but their manifestation might also occur in ways not pictured. Currently, there is little understanding of the conditions present at the grain boundaries, how they vary throughout particles, and their influence on electrode performance. Evidence of dynamic boundary regions during cycling because of electrolyte penetration suggests that these regions are susceptible to chemical change.[15] Here we do not quantify the nature of the grain boundary because 2D analysis prohibits doing so but suggest that the manifestation of these boundaries and changes in their composition and structure are linked to relative crystal orientations.

Crystal orientations relevant to Li⁺ transport within NMC materials can be described by the c axis vector direction shown in Figure 3A. The plane orthogonal to the c axis facilitates Li⁺ transport, whereas Li⁺ transport is prohibited in the direction of the c axis. Equation 1 can be used to extract the c axis vector by assigning the column

Orientation Description

Global Grain Orientations

Relative Grain Orientations

Impact of Anisotropic Diffusion Ignoring Boundary Effects

Figure 3. Grain Orientation Characterization and Effect

(A) Representation of the hexagonal structure of an NMC cathode. Li^+ travels in-plane on the green layer. The c and c_2 axes are equivalent.

(B) 12 symmetries exist in the considered hexagonal system. Numbers and shading are used to clarify the rotation/mirroring from the original position.

(C) The crystal c axis represents the transport plane orientation with a single vector. Azimuth (θ) and elevation (φ) angles can represent the direction of the c axis and, thus, the orientation of the transport plane.

(D) 3D polar histogram representing orientation distributions of the c axis. Frequency of orientation is proportional to radial length. Two hypothetical particles are imagined; on the left is one with all grains randomly oriented and on the right one that has several preferred orientations. More details about the 3D histogram are provided in the Supplemental Experimental Procedures and Figure S8. The tool is uploaded at https://github.com/NREL/FIB-SEM-EBSD-particle-scale-analysis.

(E) Some potential Li^+ transport mechanisms.

(F) Measurement of crystal orientation relative to the radial direction (r-orientation).

(G) Grain misorientations (g-misorientations). g_1 and g_2 are the c axis orientations for neighboring grains. b1 and b2 are two differently oriented grain boundary planes.

(H) Example of anisotropic diffusion in a contrived example. Arrows indicate increasing time (Note S1).

vector $[x\ y\ z]^T$ as the unit c axis vector $[0\ 0\ 1]^T$. This assignment results from the convention established in the EBSD OIM Analysis v.8 (EDAX, USA) software, where the c axis aligns with the z' axis of the crystal coordinate system. Because NMC has a hexagonal unit cell, multiple orientations of the crystal are considered equivalent (Figure 3B). This means the c axis vector in Figure 3A has one equivalent rotation in the opposite direction (the c_2 axis). This is an approximation for the purposes of considering only the planes through which Li^+ travels.

The orientation of the c axis can be described with spherical coordinates to represent the orientation of the Li^+ transport plane in a grain (Figure 3C). A 3D spherical histogram, shown in Figure 3D, was used to bin the direction of each pixel in a representation akin to a 2D polar histogram. Bins extended further from the origin have more pixels with their c axis orientated in that direction. Because each c axis rotation has two equivalent directions, a hemisphere on the 3D histogram describes all possible orientations of the c axis. Crystals with higher symmetry might require an even smaller portion of the sphere to represent all possible rotations. Figure 3D shows two hypothetical NMC samples. The hypothetical sample described by the left column has its crystals oriented uniformly in all directions. The right column represents another particle with a non-uniform distribution of grain orientations.

The orientation distributions represented in Figure 3D are relative to the fixed Cartesian sample coordinate system. This visual representation determines the degree to which grains are oriented in the same direction in the Cartesian reference. Inhomogeneities found using this 3D histogram do not necessarily inform one about the effect on lithiation because of grain orientations; for example, if all grains are oriented inward, then the distribution of grains is uniform, like in the right column of Figure 3D. The 3D histogram can still hint at the structure formed by a specific synthesis. If all grains are oriented in the same direction, meaning a single bin protrudes from the histogram, then this might suggest that all grains expand anisotropically in the same directions, and stresses are minimized. Such visualization would quickly suggest whether single-orientation particles were created and the primary direction of diffusion and highlight the facets of the particle that promote intercalation.

The orientation of grains relative to the particle center better indicates accessibility of Li^+ to grains during inward lithiation of the particle from the surface. Several scenarios are possible, depending on the orientation and transport characteristics of the boundary regions (Figure 3E). If boundary transport is slow, then crystal orientations may create tortuous paths and locally concentrate Li^+, causing inhomogeneous redox of NMC. Grains oriented inward may allow easier access of Li^+ throughout the entire particle. In another case, relatively fast transport at boundaries may allow equal access of Li^+ to all grain surfaces. Additionally, grain boundary defects or different types of grain boundaries may impede or facilitate transport at different locations.

Expressing the grain orientation relative to the particle center requires locating the center, as depicted in Figure 3F. The best representation of the 3D center of the particle may not be in the 2D slice acquired through EBSD but, rather, may lie deeper in the sample or in an already milled slice of the particle. With knowledge of the particle center, the r-orientation can be calculated using Equation 3, where a and b are two unit vectors representing (a) the c axis grain orientation at that position and (b) the particle radial direction to that position. This produces the same result as $\theta = \cos^{-1}(a \cdot b)$ but with better numerical accuracy. Two example angles are shown in Figure 3F. For transport, the best angle is $90°$, which corresponds to Li^+

transport planes parallel to the radial direction. The worst case is 0°, corresponding to transport perpendicular to the particle radius.

$$\theta = 2\tan^{-1}\left(\frac{\|(a\bullet\|b\| - b\bullet\|a\|)\|}{\|(a\bullet\|b\| + b\bullet\|a\|)\|}\right) \qquad \text{(Equation 3)}$$

Relative orientation measurements between adjacent grains, or misorientations, may also provide insight into the transport properties at these boundaries. Typical misorientation representations rely on a rotation axis that is common between the two crystals, which is difficult to interpret in the context of transport.[66] The approach used here was to measure the c axis misorientation using Equation 3, where a and b instead refer to the c axis directions of two neighbor grains. This is visualized in Figure 3G with the g-misorientation, showing an angle more representative of Li^+ transferability between boundaries. A large angle implies that the layers of two grains are aligned so that transfer of Li^+ from one grain into the other is impeded. Low angles imply that Li^+ can readily move between grains. Care must be applied to this method specifically because of the boundary plane. As shown in the bottom section of Figure 3G, the boundary plane relative to the crystal will partially determine whether Li^+ can hop between grains. In the extreme case, the boundary plane location relative to the c axis direction of one grain can impede Li^+ transport. This is shown at the bottom of Figure 3G where, regardless of the orientation of g_2, Li^+ transport across the boundary does not occur. This highlights the importance of quantifying the boundary topology.

The effect of grain orientation is difficult to quantify without more experiments, but we can estimate its effect assuming boundary and bulk grain behavior. A contrived diffusion model to demonstrate heterogeneous concentration because of grains of varied orientation is shown in Figure 3H. In the simulation, the x and y direction diffusion coefficients vary by two orders of magnitude. This is a reasonable and potentially low estimate of the difference in through-plane and in-plane diffusion. Although a different system, diffusion in planar graphite can vary in orders of magnitude where through-plane diffusion occurs at hole-type defects in the graphene sheets.[67] To our knowledge, anisotropic diffusion coefficients for NMC cathodes have not been measured. Another simple model of a single particle suggests that, in the absence of all anode and resistance overpotentials, the charge rate of 10-μm-diameter cathode particles is highly sensitive to order-of-magnitude changes in the solid-state diffusion coefficient D_s (Note S2; Figure S2). This model might predict the maximum improvement in charging because of increased D_s, which may act as a proxy to grain orientation if boundary behavior can be neglected. More detailed simulations could focus on charge rate dependence on heterogeneous and anisotropic transport, including realistic overpotentials and incorporation of enhanced and/or impeded boundary transport.

Grain and Intra-grain Crystallite Identification

Grain size and morphology also affect transport. Small grains result in more grain boundaries. Morphology affects the grain boundary topology, which might affect cross-grain Li^+ transport. Thus, we quantified morphology and relative grain orientations. Grain morphology, inter-grain orientation, and similar features for intra-grain regions (which contain crystallites) were extracted using the method outlined in Figure 4. The first step was to identify grains, background, and boundary regions using machine learning-based segmentation where, effectively, low-IQ regions were classified as boundaries. IQ maps were used for segmentation for two reasons. First, segmentations of the SEM image (Figure 1) produced irregularly shaped grains because of low contrast or unidentifiable boundaries. Grain boundary size, grain orientation, boundary plane orientation, and the ways in which the electron beam
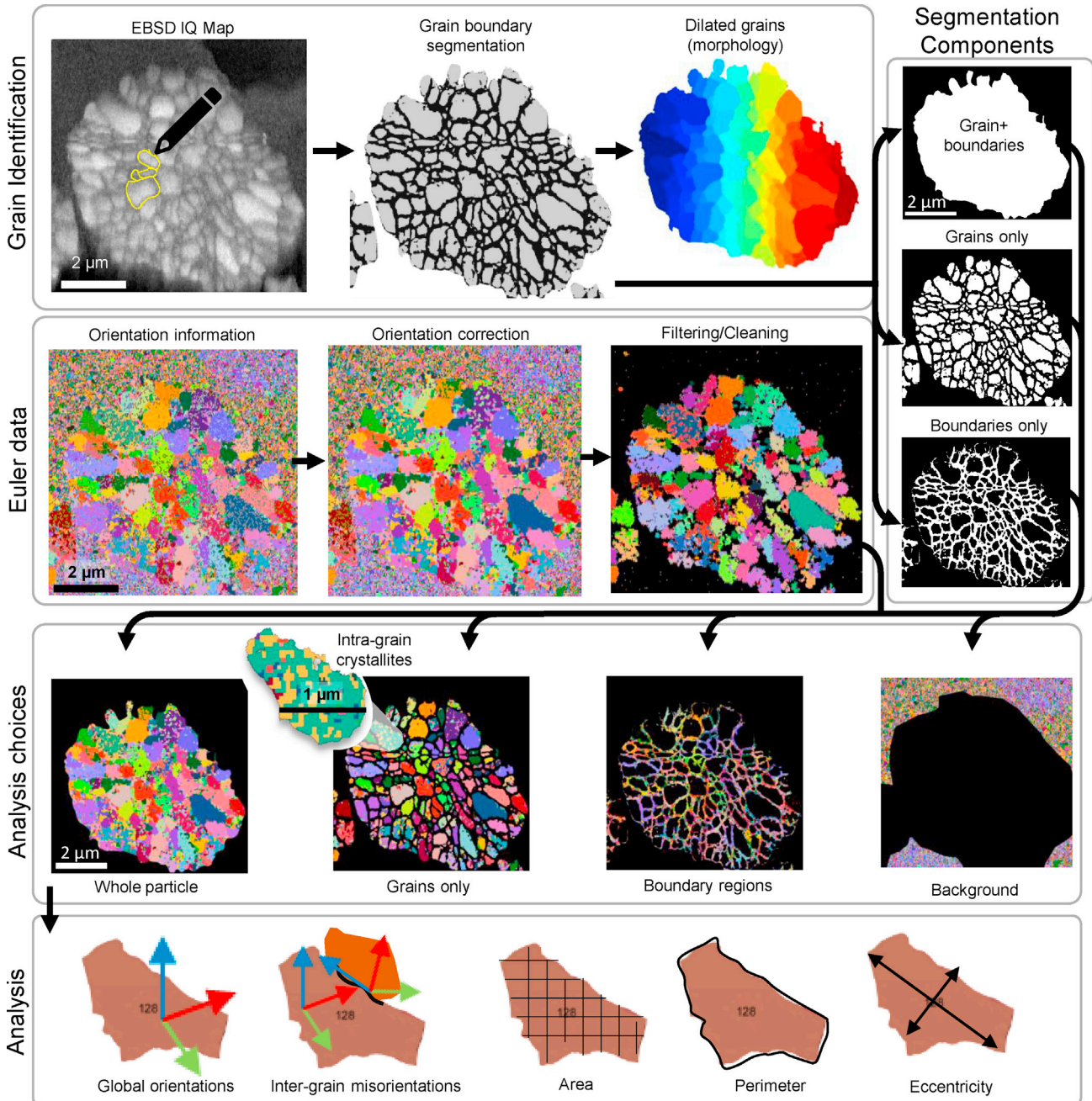
Figure 4. Flowchart of EBSD Data Processing Prior to Grain and Intra-grain Analyses
Coloring is for visual distinction of grains. Dilated grains were used for morphology. Whole-particle EBSD data were used for grain orientation analysis, using segmentation components as masks.

interacts with boundaries determine which boundaries produce high contrast. Second, the orientation information extracted from EBSD in boundary regions was not reliable enough to rely solely on grouping alike orientations with Euler data, a typical method with EBSD.

The segmentation was processed to remove artifacts of the segmentation (e.g., tiny grain, boundary, and background regions) and to dilate grains into the boundary

region to account for the artificial thickening of the boundary regions by the segmentation (Figure S9). This resulted in labeled grains with touching boundaries used to calculate morphology. The true boundary region in these uncycled samples was expected to be much smaller than the resolution of the EBSD measurements (in FIB SEM images, boundaries had no discernable thickness). Multiple effects can change the apparent or true thickness of the grain boundary; EBSD patterns are spatially averaged and difficult to deconvolute at or near boundaries, exposed boundary surfaces can degrade, and the segmentation method can vary. High-IQ regions classified as grains sometimes included intra-grain crystallites, which were typically indistinguishable in SEM images and the IQ map. Intra-grain crystallites were labeled by grouping adjacent and similarly orientated pixels (Figure S10).

Noise removal was applied to the EBSD data. Sophisticated methodologies exist for noise removal and grain boundary identification.[68] Here we applied a simple size filter to replace clusters of pixels of less than 0.01 μm^2 (often speckles of this size were of apparent random orientation and near the resolution limit of 50 nm or 0.0025 μm^2) with the orientation of nearby pixels prior to orientation analysis (Figure S10). The segmentation components acted as masks to evaluate different regions of the EBSD data. Grain area, perimeter, and eccentricity (the ratio of the distance between the foci of the ellipse, formed with the same second moment as the grain, and its major axis length; 0 is a circle, and 1 is a line segment) were calculated through morphology analysis of the labeled grains using the "regionprops" function in MATLAB.

The process just described has multiple sources of potential error. The segmentation is susceptible to user error. An example of segmentation reproducibility because of user input is given in Figure S7. IQ values depend on instrumentation, processing software, sample material, and sample preparation, meaning that these conditions must be considered when applying segmentation techniques. The boundary region in the segmentation is roughly 100–200 nm thick, potentially affecting grain areas by shells of that thickness. EBSD data are masked with the segmentation. Morphology calculations depend on the segmentation and the subsequent cleaning/dilation procedures. Thus, when segmentation is applied to 3D for quantitative comparisons between particle architectures, sensitivity analyses need to be conducted. A mix of different microscopic techniques and standardization of EBSD collection and processing may be necessary to confidently classify grain boundaries and their thickness. Clear distinction of boundaries, voids, cracks, and grains will be necessary for degradation studies.

Spatial Quantification of Grain Morphologies

For simplicity of conveying the quantification technique and its output, we describe methods with 2D data despite our conclusion that 2D images are not enough to draw accurate microstructural information of the particles in Li$^+$ electrodes. The focus here is to convey the technique rather than draw conclusions regarding the particulars of the specific electrode, which will be a topic of a future study. 3D morphology is crucial for obtaining the true shape of the grains. With 2D information, the user risks assuming the grain shape when potentially unrepresentative portions of certain grains are cross-sectioned. Another important geometric feature that cannot be captured in 2D is the boundary topology. Last, we have no bearing on the centroid of the particle (an approximate general direction for lithiation). These points all have implications for measuring Li$^+$ transport when using crystal orientation and morphology information. The technique described here can be extended to 3D, but given the additional challenges of acquiring 3D data, it might be tempting for experimentalists to only acquire 2D data for quantification; for this reason, in a later
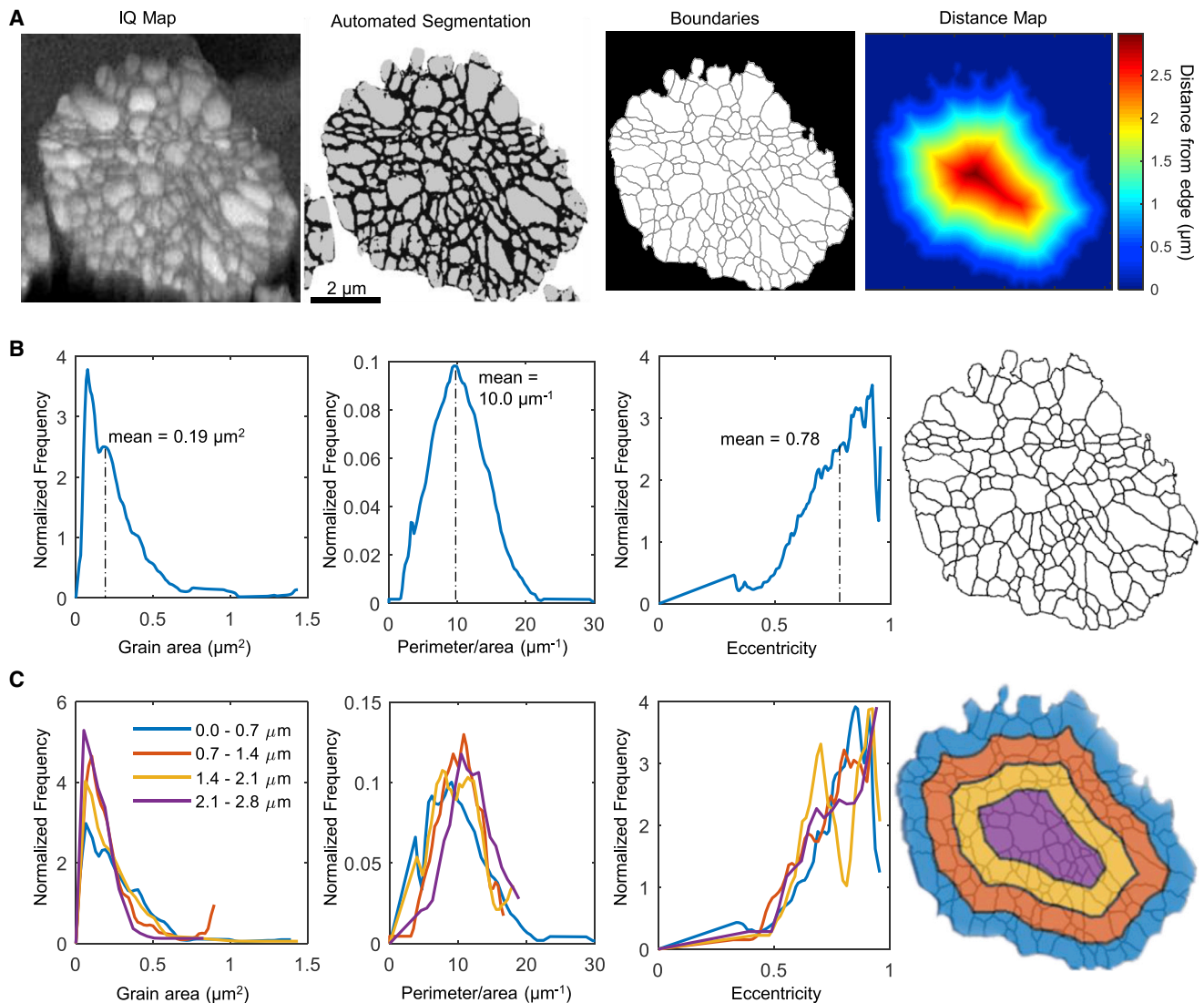
Figure 5. Grain Morphology Analysis

(A) Use of image quality (IQ) maps for segmentation and extraction of boundaries. The Euclidean distance map was generated using the distance from the particle edge.

(B) Morphological properties for all grains.

(C) Grain morphology in regions sectioned by distance from the particle edge.

The plots in (B) and (C) are normalized so that the integrated area under the curve is unity.

section, we include a discussion of the limitations of 2D measurements as well as feasible means by which 3D data can be acquired.

The major components relevant to morphology measurements are shown in Figure 5A. The segmentation from the IQ map separated grains and boundary regions. With the procedures described in Figure S9, individual grains were dilated to remove the boundary region. Using the boundary of the entire particle, a Euclidean distance map (distance from the edge of the particle) was created. Grain shape determines the boundary plane and the relative fraction of bulk to boundary regions. The width of the boundary region is currently unknown and cannot be estimated with EBSD. In Figure 5B, the overall frequency distribution of three morphology

indicators are plotted. The same indicators were plotted for four regions based on distance from the particle edge (Figure 5C). The perimeter/area ratio is a 2D equivalent of the 3D specific surface area, which affects the balance of interfacial to bulk grain transport. Last, the eccentricity may indicate whether grains are elongated in a specific crystallographic direction, affecting the facets available for Li^+ intercalation. These morphological measurements are basic examples. The small dataset precludes conclusions relating grain morphology to their distance from the particle edge.

Spatial Quantification of Orientations

Orientation distributions with respect to the Cartesian sample coordinate are shown in Figure 6. In Figures 6A and 3D, histograms represent grain orientations relative to the sample coordinate for the entire particle cross-section; in Figure 6B, the grains excluding the boundary regions; in Figure 6C, the boundary regions alone; and in Figure 6D, the background surrounding the particle. Each pixel in the region of interest is counted in the 3D histogram with the same weight. The particle does not have a uniform distribution of grain orientations. The same is shown for only the grains. The boundary region displays preferential orientations in one direction although with low IQ. Oddly, the noisy EBSD data in the background exhibit a slight preference in orientation, but no confidence in the observed orientation can be assigned to this region. Unfortunately, the 2D cross-section analysis neglects the volume of individual grains. Assuming that the cross-sectional orientation information represents an entire particle, the effect of orientation on transport should be weighted more for grains closer to the edge of the particle because the volume covered by a surface element in a sphere increases with radial distance. Ideally, 3D analysis would be used to obtain voxel-resolved orientation information for the entire particle.

The distribution of c axis r-orientations, as illustrated in Figure 3F, was quantified. Figure 7A demonstrates the geometric considerations and assumptions for this calculation. Assuming a spherical particle and using knowledge of the particle size distribution and mean diameter (d10, d50, d90 = 7.1, 9.3, 12.1 µm), the average particle cross-sectional diameter was used to estimate the distance from the slice to the particle center (r_{offset}). The 3D vector from the particle center to each grain (r_{real}) was then calculated by addition of r_{offset} with the distance to each pixel from the particle centroid (r_{image}). The angle between the vector r_{real} and the c axis angle of the grain is the r-orientation (Figure 7B). Figure 7A shows that the cross-section can be in two possible locations relative to the EBSD detector: above and below the particle center. Results for both cases are shown in Figures 7C and 7D for slices 1 and 2, respectively. The error bars are the same calculation done for the d10 and d90 particle diameters. The histogram shape changes based on the assumption of the slice location because, even though the grain orientation relative to the EBSD detector is the same, the grain orientation relative to the radial direction (r_{real}) changed. The error bars result from uncertainty in the location of the EBSD cross section relative to the particle center because of the distribution of known particle sizes in the cathode. In both cases, the grain orientations are random relative to the radial orientation. The distribution of random orientations (in Figures 7 and 8) were created by generating many pairs of randomly oriented vectors and calculating the angle between them. Better radial transport might be achieved with a greater proportion of the grains having r-orientations of 90°. Ideally, for intercalation, the maps in Figures 7C and 7D would be all black, indicating that all grains lead Li^+ directly toward the particle center. However, without exact knowledge of the particle center, the exact r-orientation distributions cannot be made. Tracking of the milled distance
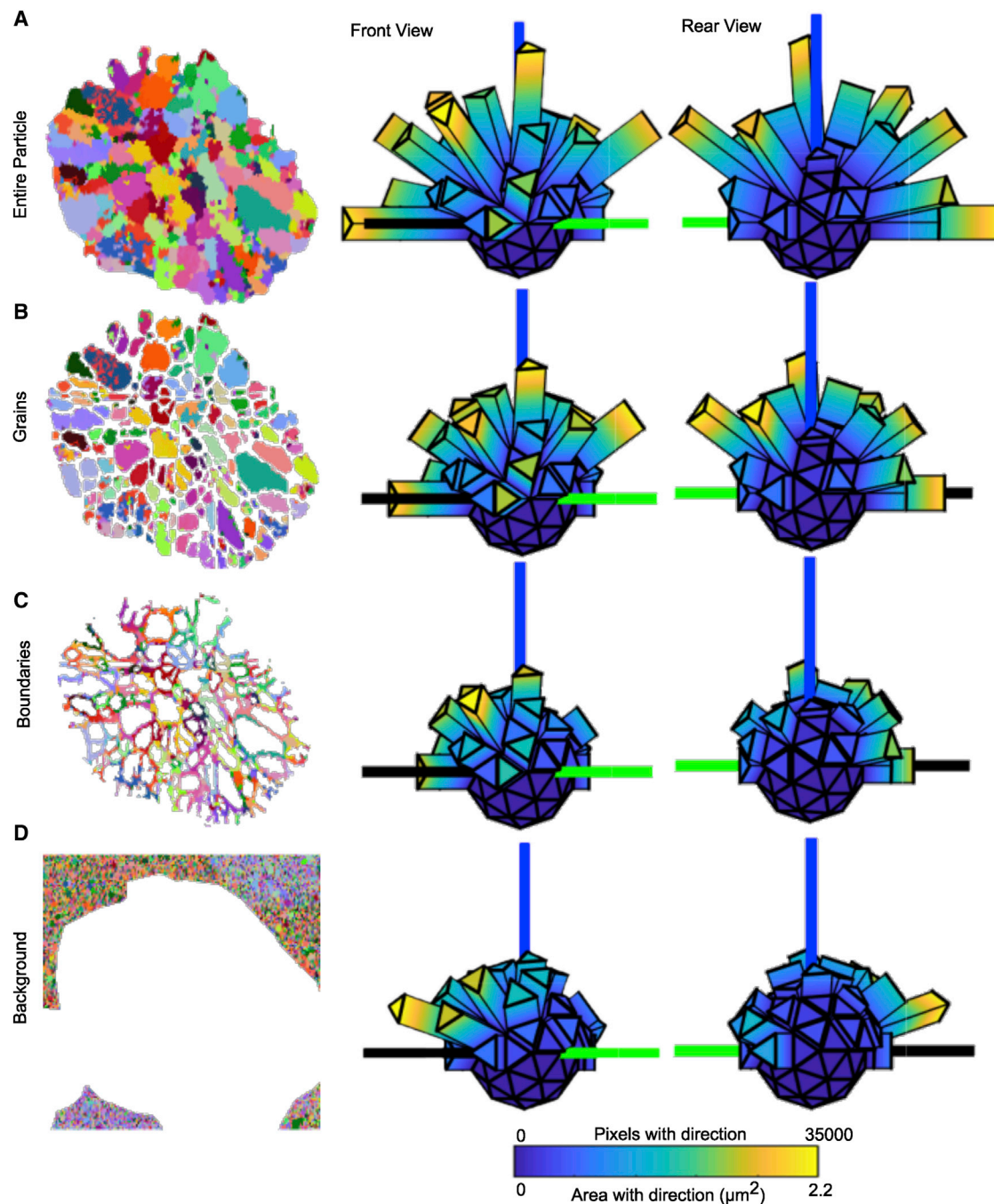
Figure 6. Global Orientations

(A–D) Grain orientation distributions measured with *c* axis orientation using 3D histograms for the following regions: (A) the entire particle, (B) grains only, (C) boundaries only, and (D) the background surrounding the particle. Coloring in the left column is only for visual distinction of grains. The middle and right columns are the front and rear views of the same histogram.

and the particle area would allow an accurate r_{real} to be measured; near the particle center, the area is largest, and the change in area with milled distance is lowest. Extension to 3D would allow better estimates of this parameter or defining the centroid as the particle center. The histograms in Figures 7C and 7D should be created with voxels instead of pixels to volume-weight the r-orientation.
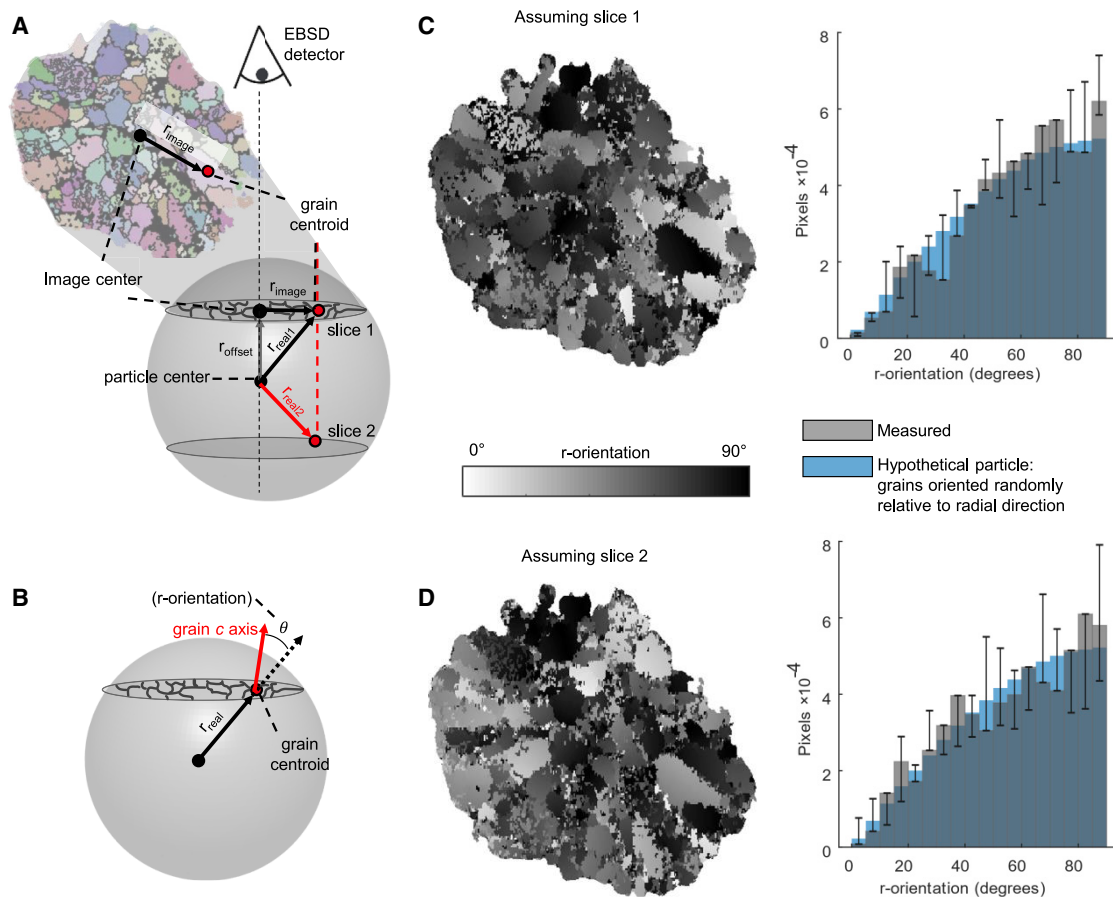
Figure 7. Orientation Description Relevant to Radial Transport

(A) Geometric considerations for calculating r_{real}, the radial direction of the particle that intersects a given pixel, using a distance measured on the EBSD image (r_{image}) and an estimated distance of the image from the particle center (r_{offset}). The EBSD image was taken at 2 hypothetical slices (1 and 2). (B–D) The angle between r_{real1} or r_{real2} and the c axis of each grain is the r-orientation (B), the histogram of which is shown in (C) for slice 1 and (D) for slice 2. Darker colors indicate better c axis alignment for radial transport of Li^+ in the color-mapped cross-section. (C) and (D) assume that the particle diameter equals the d50 diameter, and error bars are the same calculation for the d10 and d90 particle diameters. Error bars are for the measured data.

Although there is still some uncertainty regarding how Li^+ transfers from one grain to the next, it is likely that the relative orientation of the neighboring grains have an effect. The relative g-misorientation was calculated for all boundaries, those between grains, and those between intra-grain crystallites in Figures 8A–8C, respectively. Grain boundaries were identified where adjacent pixels had different orientations. Two significant features at 5° and 70° dominated the histogram of g-misorientations comparing all boundaries (Figure 8A). Focusing on the grain boundary regions demonstrated a random distribution of g-misorientations (Figure 8B). The slight dominance in low angle misorientation (<5°) might be attributed to the same grains (EBSD resolution can vary based on sample and instrumentation quality and, for clean samples, is usually reported with 0.1°–1° accuracy). In addition, grains that gradually change orientation might be difficult to identify with EBSD.[48] By focusing on regions of high IQ (avoiding the inter-grain boundaries), the 70° feature was accentuated (Figure 8C). The high IQ suggests that these boundaries are well-defined, unlike the inter-grain boundaries, and, thus, may have different properties. Such boundaries might be due to thermodynamically preferable grain twinning, as
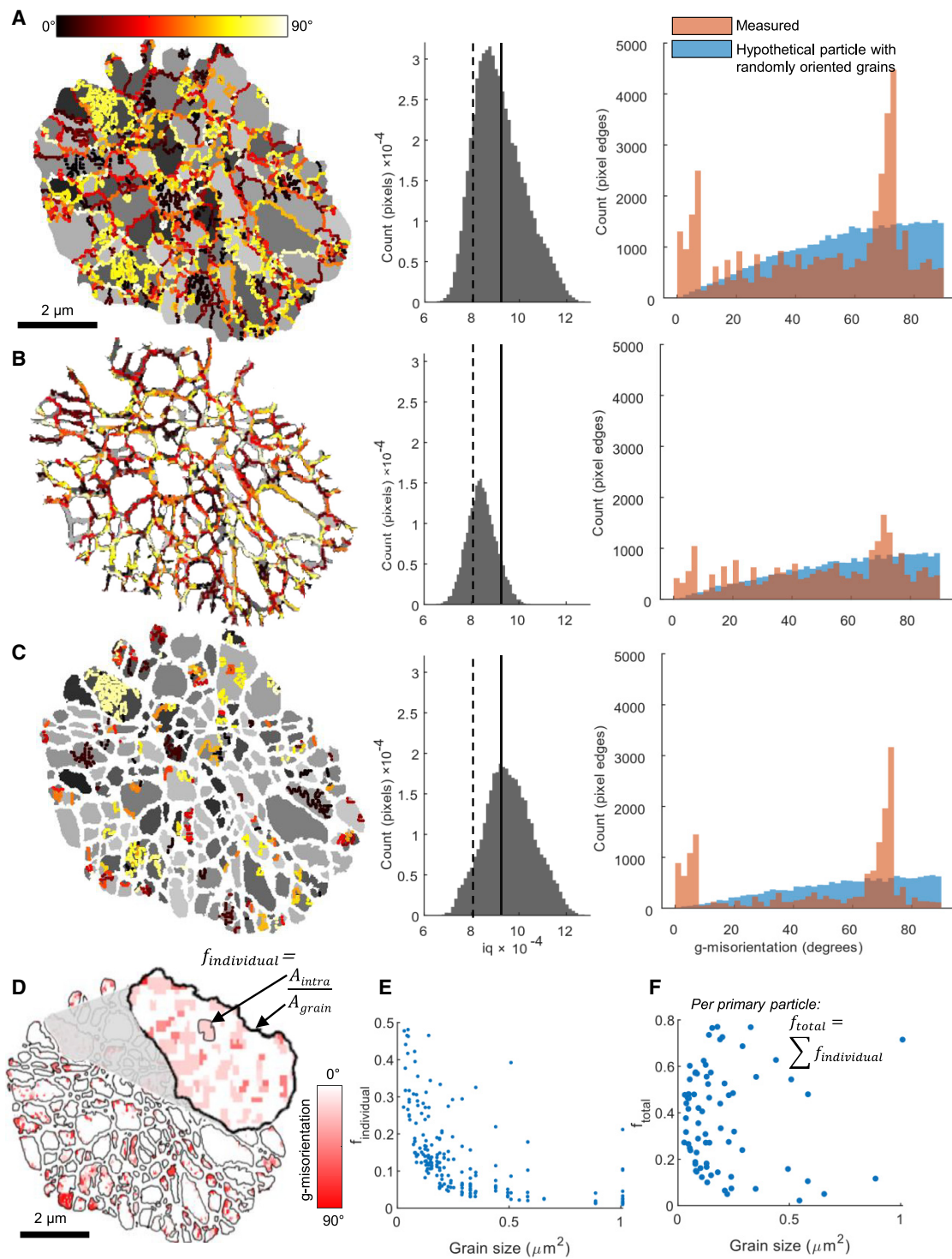
Figure 8. Grain and Crystallite Boundary Misorientations

(A–C) Color-coded g-misorientations on boundaries (left panels), histograms for IQ values in regions shown (center panels), and misorientation histograms (right panels) for (A) all boundaries in the particle, (B) inter-grain, and (C) intra-grain. Solid and dotted lines in the IQ histograms are visual guides. The blue histograms are simulated distributions with many randomly oriented grains.

(D) Colorized misorientation. Darker shades of red represent a higher misorientation angle between the most frequent grain orientation and the crystallites contained within.

(E) Scatterplot where points represent the fraction of the area occupied by each intra-grain crystallite.

(F) Scatterplot where points represent the collective area occupied by all intra-grain crystallites within a grain.

described by the coincident site lattice (CSL) model.[69,70] Although twin boundaries exhibit lower surface energies than other boundaries, their formation depends on the boundary plane, which cannot be measured in 2D cross-sections, supporting our assertion that 3D studies are needed.[71] A non-planar boundary may also invalidate the CSL theory. Nevertheless, their predominance might be important when considering transport and degradation. A similar 70° feature measured with a different technique was reported recently in NMC.[48]

Because boundary regions often have lower-quality data, we also assumed that the boundary region had the same orientation as the bulk of the grain. The g-misorientation was then calculated using the bulk grain orientation rather than those found originally at boundaries (Figure S3). This might better describe boundaries, especially because EBSD performs relatively poorly in the boundary regions. Similar data cleaning might need to be performed in 3D datasets.

The presence of intra-grain crystallites potentially affects Li^+ transport. Thus, their frequency was estimated by measuring the relative area of grains occupied by intra-grain crystallites oriented in the non-predominant orientation of that grain (Figures 8D–8F). In Figure 8D, the orientation data are colored so that the white color in each grain is the most common direction, and darker shades of red indicate larger g-misorientations. The coloring demonstrates that some grains are a single crystallite, whereas others consist of multiple crystallites. Disconnected crystallites within the same grain often have the same orientation. Generally, the areal occupation of individual intra-grain crystallites was less than 10% of the total area (Figure 8E). A significant fraction of grains contains more than 50% intra-grain crystallites by area (Figure 8F). Our presented evidence and previous studies suggest that grains generally exhibit long-range order but have substantial flaws or defects.[48] The nature of Li^+ transport in the presence of such defects requires more study.

Limitations of 2D Measurements and Moving to 3D Application

Quantification of properties relevant to Li^+ transport in polycrystalline electrodes (grain orientations and morphology) requires 3D data acquisition as well as 3D segmentation and quantification techniques. Relative grain orientations are obtainable from 2D EBSD, but, we emphasize, further transport analysis is restricted by assumptions regarding the particle and grain morphology. The long-term goal is to answer how the combination of grain morphology and grain orientation distribution, in concert, affect Li^+ transport and, ultimately, degradation. Using only 2D data, deviations of the actual from the assumed morphology might lead to inaccurate 3D representations of the entire particle that might misinform transport simulation efforts. Current synthetic methods do not precisely control the morphology and grain orientation of fresh cathode particles. Thus, we cannot confidently assume 3D morphology and orientation from 2D data. The prudent approach is to accurately capture 3D particle data and then apply sensitivity analyses to processes occurring during cycling (e.g., Li^+ transport, NMC redox, mechanical stresses, and others) with respect to geometric and orientation descriptors. Deviations between experimental and simulation results might reveal whether boundaries disproportionately affect particle behavior during cycling.

Automated 3D EBSD collection is possible using systems equipped with ion milling that facilitate slice and view. However, 3D EBSD with high-enough resolution to capture the detailed morphology of grains throughout an entire particle is very time consuming. The straightforward but time-intensive method to obtaining a 3D model, which includes grain morphology and orientations, would be to collect

EBSD on many slices of a single particle (Figure 9A). Newer complementary metal oxide semiconductor (CMOS) EBSD detectors substantially speed up the data collection process. Because of the necessity for high-quality EBSD maps, this would be a highly time-consuming process, especially when comparing multiple samples. There are opportunities to optimize this process. For example, minimizing the time for EBSD while still acquiring detailed microstructural information could be achieved through high-resolution FIB SEM imaging with intermittent EBSD images (Figure 9B) or high-resolution FIB SEM with coarse EBSD imaging. The sparse EBSD data could then be used during post processing to fill the segmented grains with orientation information. There are also technical challenges to acquiring FIB EBSD of a full particle. For FIB SEM EBSD, the sample is tilted back and forth between detectors and the ion mill. Realignment for each consecutive image requires a fine and consistent fiducial marker to guide the stage position to where the sample was originally in view. Some EBSD systems already have software packages available to center on pre-milled fiducial markers. The sample also experiences a lot of electron exposure during SEM and EBSD, which may cause the sample to shift relative to the fiducial marker; hence, post-process image realignment may be required.

Full reconstruction of 3D particles with morphological and crystal orientation information would provide a wealth of data of interest to the battery community concerning grain boundaries. A previous study explored volumetric crack formation at grain boundaries and redox heterogeneity (using 3D full-field transmission X-ray microscopy and X-ray absorption near-edge spectroscopy) and quantified their effect on transport with numerical modeling, assuming isotropic diffusion and that cracking events disrupt ionic and electronic diffusion.[18] Such techniques offer useful morphology and oxidation state information but do not resolve orientations or all grain boundaries; thus, they cannot address questions related to these. EBSD introduces orientation as new information, which alters transport, predicts anisotropic grain expansion direction, and helps identify boundaries prone to degradation. Thus, our future work will apply 3D EBSD to compare the structures of different NMC materials, classify boundary types, and monitor NMC degradation under cycling. Battery cycle life could be compared with g-misorientation and r-orientation distributions to attempt to relate simple orientation parameters to architecture. Degradation may preferentially initiate and propagate at or along specific boundaries (Figure 9C). Because cracks are volumetric entities, a full understanding of their propagation behavior might only be accomplished with 3D datasets (Figure 9D). These 3D reconstructions could provide realistic datasets to simulate transport and sub-particle tortuosity and its effect on electrode performance, where grains and boundaries can be assigned different transport, thermal, and mechanical properties. This could help study the structures shown in Figure 9E. We can speculate that the left structure in Figure 9E would quickly charge/discharge but mechanically disintegrate, whereas the structure on the right would accommodate mechanical stresses but slowly charge/discharge. The extent of these effects would be the goal of model-based studies.

However, there remains uncertainty regarding the transport processes occurring at grain boundaries. The detail at the boundaries requires nanometer resolution techniques, such as transmission electron microscopy (TEM), which would help determine the different properties grain boundaries might have throughout an NMC particle. A multi-scale approach of 2D TEM and 3D EBSD could better classify grain boundaries and lead to insights into transport properties. Figure 9F demonstrates the concept where intra-grain crystallite boundaries and other inter-grain boundaries might be classified based on the boundary plane and relative grain
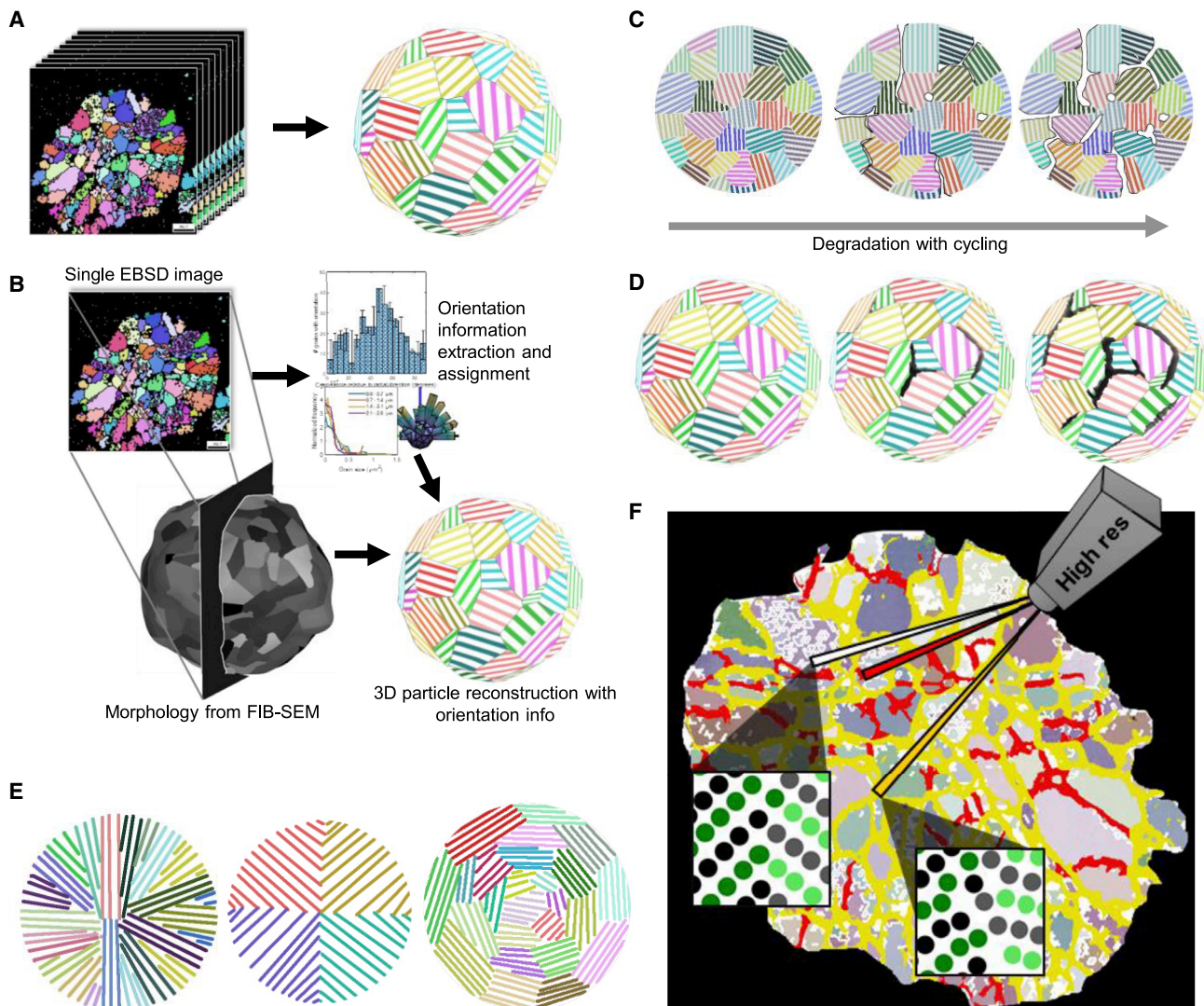
Figure 9. Necessary Future Extension of the Technique to 3D

(A) Brute force method of obtaining morphology and orientation information for a 3D particle.

(B) Example of a reduced-effort technique to obtain a 3D representation of a particle with morphological and grain orientation data.

(C) Cycling of a particle, with disintegration occurring between boundaries.

(D) 3D representation of disintegration.

(E) Examples of particle configurations to study experimentally and with simulation.

(F) Correlation of atomic structure to grain misorientations.

orientations. Two reasons for this might be to (1) map these classifications onto generated 3D polycrystalline models or (2) perform high-resolution studies of classified regions. Techniques such as high-resolution TEM could be used to clarify boundary region structures.[46,48] Electron energy loss spectroscopy can be used to obtain the elemental composition and oxidation state of the boundary region at atomic resolution[72–74] and energy dispersive X-ray spectrometry to supplement the elemental composition probing.[15] First-principles methods (e.g., DFT) can assist with study of transport rates for the various identified grain boundary configurations.[49,50]

Cross-section analyses with EBSD provided grain orientation distributions, boundary misorientation distributions, and, with limitation, morphological features. IQ maps were used to distinguish grains and their boundaries. EBSD data analysis was confined to regions based on segmentations produced from the IQ maps. The segmentation was also used to create mappings of labeled grains. First we extracted morphological features from the labeled grains and attempted to measure location-dependent morphology. Using a vector description of the Li^+ transport plane, the c axis direction, we revealed preferential misorientations between crystallites potentially related to grain twinning. The angle between c axes of neighboring grains was also used to describe their misorientation. This hinted at impeded transport throughout the particle. We highlighted that the grain boundary plane, which could not be measured with 2D EBSD, is important in determining whether Li^+ can transport across grains. Furthermore, the nature of the grain boundary and its effects on lithiation behavior are still uncertain and will require further multi-modal investigations. Another metric we highlighted was the r-orientation. This was done to measure the ease with which a particle might lithiate inward from the particle surface. Grain orientations were apparently random. Future synthesis efforts could thus focus on favorably orienting grains. The focus of this work was primarily on technique development, leaving ample opportunity for future investigations to explore the link between grain architectures and electrochemical performance of electrode particles.

Analyses like that performed here should be applied to 3D data to better understand NMC material architecture, especially to focus on features not resolved in cross-sections. Future 3D analysis of polycrystalline NMC materials might be accomplished by brute force (cross-sectional EBSD reconstruction), combined methods (morphology from SEM and orientation from EBSD), and simulation (generation of 3D morphology and grain orientations). We expect the EBSD platform to be useful for diagnostic purposes and for mechanistic transport studies. For quick materials diagnostics, the combined method of a few EBSD slices and morphology obtained via FIB SEM could be used. Detailed grain boundary analysis might be supplemented by classification of boundary types by the neighboring grains. Full 3D EBSD reconstructions could be used as a baseline for verification of the applicability of these techniques. A wealth of expertise from EBSD studies in mineralogy and metallurgy remains to be applied to Li^+ electrodes and may provide even more information in needed 3D studies.

Incorporation of orientation information into battery research might suggest ways to extend battery lifetime and improve the charge rate. EBSD studies could supplement previous studies that provided redox, strain, void, and cracking information in 3D to give complete structural pictures of particles. This structural information could help pinpoint inter-granular crack formation mechanisms by simulating anisotropic expansion and transport. New research efforts should be directed to understanding the various grain boundary types and their physical implications by correlating boundary plane and misorientations with transport and degradation. One might imagine 2-crystal model systems where specific boundaries are synthesized and studied. Low-stability boundaries may initiate degradation with mechanical perturbation. Grain boundaries may transport Li^+ more quickly than in bulk NMC, or the tortuous paths within polycrystalline particles might control transport. The specific surface area of grains could predict how often boundary-related events occur compared with bulk effects. Evaluating grain orientation distributions, misorientations, and morphology is a crucial step to answering how sub-particle architecture affects battery performance.

EXPERIMENTAL PROCEDURES

Resource Availability

Lead Contact

Further information and requests for resources and reagents should be directed to and will be fulfilled by the Lead Contact, Donal P. Finegan (donal.finegan@nrel.gov).

Materials Availability

This study did not generate new unique reagents.

Data and Code Availability

The authors declare that data supporting the findings of this study are available upon request from the authors, the code used in this work is available on the National Renewable Energy Laboratory (NREL) GitHub, and a detailed description of the steps taken to process the data is provided throughout the Supplemental Information. The code generated during this study is available at https://github.com/NREL/FIB-SEM-EBSD-particle-scale-analysis. Any further information can be acquired from the authors upon request.

Materials

An uncycled cathode sample was argon-milled with a JEOL CP ion beam cross section polisher (JEOL, USA). The calendared cathode consisted of TODA Kogyo Corporation $LiNi_{0.5}Mn_{0.2}Co_{0.2}O_2$ (NMC532) particles that were integrated into a 70-μm-thick electrode coating of 90 wt% NMC532, 5 wt% C45 Timcal conductive carbon, and 5 wt% polyvinylidene fluoride (PVDF) binder on a 20-μm-thick aluminum current collector. The composite cathode was used to show that commercial electrodes can be studied without further processing. Particles separated from the binder material could also be used if bonded to a conductive surface, and the results are expected to not change unless calendaring or other processing highly stressed particles, which may be a study of interest to manufacturers. The polished cross-sectioned electrode was kept inside an Ar-filled glovebox for about a day until the cross-sections were analyzed.

Methods

SEM and EBSD images were acquired with an FEI Nova NanoSEM 630 equipped with an EDAX EBSD detector. SEM quality was poor because of low electrical conductivity of the sample. Better sample preparation can improve SEM images and EBSD data. In each cross-section, multiple particles were screened, and a single particle was selected to image at higher SEM resolution. EBSD data were subsequently acquired for the same sample in step sizes of 50 nm. EBSD data were processed with OIM Analysis v.8 (EDAX, USA). Diffraction patterns were fit to a trigonal crystal system (space group R-3 m) with a = b = 2.875 Å and c = 14.248 Å to obtain the orientation of the crystal at each pixel (a, b, and c are the edge lengths of the hexagonal unit cell that contains the trigonal structure; Figure 2A). The software produced text files containing a spatially resolved confidence index, IQ, and Bunge-Euler angle data (Figure S4).

IQ maps in Tagged Image File Format (TIFF) format were created in MATLAB. Segmentations of the TIFF IQ maps were performed with the Waikato Environment for Knowledge Analysis (Weka) Segmentation plugin included in the Fiji distribution of ImageJ 1.52p.[75] In the software, between 3–5 regions corresponding to the defined grain, background, and boundary classes were hand-selected as training data, allowing the remaining image pixels to be classified. Figures S5–S7, and S9 provide more detail on the segmentations. The MATLAB code and data used

in analysis and visualization are available at https://github.com/NREL/FIB-SEM-EBSD-particle-scale-analysis.

AUTHOR CONTRIBUTIONS

Conceptualization, A.Q. and D.P.F.; Methodology, A.Q. and D.P.F.; Formal Analysis, A.Q. and D.P.F; Investigation, A.Q.; Resources, D.P.F.; Writing—Original Draft, A.Q. and D.P.F.; Writing—Review & Editing, A.Q., D.P.F., F.U.-V., K.S., and A.V.; Supervision, D.P.F.; Funding Acquisition, D.P.F., K.S., M.K.

DECLARATION OF INTERESTS

The authors declare no competing interests.

REFERENCES

1. Nitta, N., Wu, F., Lee, J.T., and Yushin, G. (2015). Li-ion battery materials: present and future. Mater. Today *18*, 252–264.

2. Xu, L., Zhou, F., Liu, B., Zhou, H., Zhang, Q., Kong, J., and Wang, Q. (2018). Progress in Preparation and Modification of LiNi0. 6Mn0. 2Co0. 2O2 Cathode Material for High Energy Density Li-Ion Batteries. Int. J. Electrochem. *2018*.

3. Kim, S., Wee, J., Peters, K., and Huang, H.-Y.S. (2018). Multiphysics coupling in lithium-ion batteries with reconstructed porous microstructures. J. Phys. Chem. C *122*, 5280–5290.

4. Wang, Y., Fu, X., Zheng, M., Zhong, W.H., and Cao, G. (2019). Strategies for building robust traffic networks in advanced energy storage devices: A focus on composite electrodes. Adv. Mater. *31*, e1804204.

5. Huang, C., and Grant, P.S. (2018). Coral-like directional porosity lithium ion battery cathodes by ice templating. J. Mater. Chem. A Mater. Energy Sustain. *6*, 14689–14699.

6. Mistry, A.N., and Mukherjee, P.P. (2019). Probing spatial coupling of resistive modes in porous intercalation electrodes through impedance spectroscopy. Phys. Chem. Chem. Phys. *21*, 3805–3813.

7. Forouzan, M.M., Mazzeo, B.A., and Wheeler, D.R. (2018). Modeling the effects of electrode microstructural heterogeneities on Li-ion battery performance and lifetime. J. Electrochem. Soc. *165*, A2127–A2144.

8. Lagadec, M.F., Zahn, R., Müller, S., and Wood, V. (2018). Topological and network analysis of lithium ion battery components: the importance of pore space connectivity for cell operation. Energy Environ. Sci. *11*, 3194–3200.

9. Xu, Z., Jiang, Z., Kuai, C., Xu, R., Qin, C., Zhang, Y., Rahman, M.M., Wei, C., Nordlund, D., Sun, C.-J., et al. (2020). Charge distribution guided by grain crystallographic orientations in polycrystalline battery materials. Nat. Commun. *11*, 83.

10. Wu, S.-L., Zhang, W., Song, X., Shukla, A.K., Liu, G., Battaglia, V., and Srinivasan, V. (2012). High rate capability of Li (Ni1/3Mn1/3Co1/3) O2 electrode for Li-ion batteries. J. Electrochem. Soc. *159*, A438–A444.

11. Verma, A., Smith, K., Santhanagopalan, S., Abraham, D., Yao, K.P., and Mukherjee, P.P. (2017). Galvanostatic intermittent titration and performance based analysis of LiNi0. 5Co0. 2Mn0. 3O2 cathode. J. Electrochem. Soc. *164*, A3380–A3392.

12. Doyle, M., Fuller, T.F., and Newman, J. (1993). Modeling of galvanostatic charge and discharge of the lithium/polymer/insertion cell. J. Electrochem. Soc. *140*, 1526.

13. Yan, P., Zheng, J., Gu, M., Xiao, J., Zhang, J.-G., and Wang, C.-M. (2017). Intragranular cracking as a critical barrier for high-voltage usage of

layer-structured cathode for lithium-ion batteries. Nat. Commun. *8*, 14101.

14. Min, K., and Cho, E. (2018). Intrinsic origin of intra-granular cracking in Ni-rich layered oxide cathode materials. Phys. Chem. Chem. Phys. *20*, 9045–9052.

15. Yan, P., Zheng, J., Liu, J., Wang, B., Cheng, X., Zhang, Y., Sun, X., Wang, C., and Zhang, J.-G. (2018). Tailoring grain boundary structures and chemistry of Ni-rich layered cathodes for enhanced cycle stability of lithium-ion batteries. Nat. Energy *3*, 600–605.

16. Liu, H., Wolf, M., Karki, K., Yu, Y.-S., Stach, E.A., Cabana, J., Chapman, K.W., and Chupas, P.J. (2017). Intergranular cracking as a major cause of long-term capacity fading of layered cathodes. Nano Lett. *17*, 3452–3457.

17. Ryu, H.-H., Park, K.-J., Yoon, C.S., and Sun, Y.-K. (2018). Capacity fading of Ni-rich Li [Ni x Co y Mn1–x–y] O2 (0.6 ≤ x ≤ 0.95) cathodes for high-energy-density lithium-ion batteries: bulk or surface degradation? Chem. Mater. *30*, 1155–1163.

18. Besli, M.M., Xia, S., Kuppan, S., Huang, Y., Metzger, M., Shukla, A.K., Schneider, G., Hellstrom, S., Christensen, J., and Doeff, M.M. (2018). Mesoscale chemomechanical interplay of the LiNi0. 8Co0. 15Al0. 05O2 cathode in solid-state polymer batteries. Chem. Mater. *31*, 491–501.

19. Mao, Y., Wang, X., Xia, S., Zhang, K., Wei, C., Bak, S., Shadike, Z., Liu, X., Yang, Y., and Xu, R. (2019). High-Voltage Charging-Induced Strain, Heterogeneity, and Micro-Cracks in Secondary Particles of a Nickel-Rich Layered Cathode Material. Adv. Funct. Mater. *29*, 1900247.

20. Hu, E., Lyu, Y., Xin, H.L., Liu, J., Han, L., Bak, S.-M., Bai, J., Yu, X., Li, H., and Yang, X.-Q. (2016). Explore the effects of microstructural defects on voltage fade of Li-and Mn-rich cathodes. Nano Lett. *16*, 5999–6007.

21. Balke, N., Jesse, S., Morozovska, A.N., Eliseev, E., Chung, D.W., Kim, Y., Adamczyk, L., García, R.E., Dudney, N., and Kalinin, S.V. (2010). Nanoscale mapping of ion diffusion in a lithium-ion battery cathode. Nat. Nanotechnol. *5*, 749–754.

22. Xia, S., Mu, L., Xu, Z., Wang, J., Wei, C., Liu, L., Pianetta, P., Zhao, K., Yu, X., Lin, F., et al. (2018). Chemomechanical interplay of layered cathode materials undergoing fast charging in lithium batteries. Nano Energy *53*, 753–762.

23. Sun, G., Sui, T., Song, B., Zheng, H., Lu, L., and Korsunsky, A.M. (2016). On the fragmentation of active material secondary particles in lithium ion battery cathodes induced by charge cycling. Extreme Mech. Lett. *9*, 449–458.

24. Zhang, Y., Zhao, C., and Guo, Z. (2019). Simulation of crack behavior of secondary particles in Li-ion battery electrodes during lithiation/de-lithiation cycles. Int. J. Mech. Sci. *155*, 178–186.

25. Liu, Y.-M., G Nicolau, B., Esbenshade, J.L., and Gewirth, A.A. (2016). Characterization of the cathode electrolyte interface in lithium ion batteries by desorption electrospray ionization mass spectrometry. Anal. Chem. *88*, 7171–7177.

26. Lin, F., Markus, I.M., Nordlund, D., Weng, T.-C., Asta, M.D., Xin, H.L., and Doeff, M.M. (2014). Surface reconstruction and chemical evolution of stoichiometric layered cathode materials for lithium-ion batteries. Nat. Commun. *5*, 3529.

27. Tian, C., Xu, Y., Nordlund, D., Lin, F., Liu, J., Sun, Z., Liu, Y., and Doeff, M. (2018). Charge Heterogeneity and Surface Chemistry in Polycrystalline Cathode Materials. Joule *2*, 464–477.

28. Finegan, D.P., Vamvakeros, A., Tan, C., Heenan, T.M.M., Daemi, S.R., Seitzman, N., Di Michiel, M., Jacques, S., Beale, A.M., Brett, D.J.L., et al. (2020). Spatial quantification of dynamic inter and intra particle crystallographic heterogeneities within lithium ion electrodes. Nat. Commun. *11*, 631.

29. Yan, P., Zheng, J., Chen, T., Luo, L., Jiang, Y., Wang, K., Sui, M., Zhang, J.-G., Zhang, S., and Wang, C. (2018). Coupling of electrochemically triggered thermal and mechanical effects to aggravate failure in a layered cathode. Nat. Commun. *9*, 2437.

30. McGrogan, F.P., Bishop, S.R., Chiang, Y.-M., and Van Vliet, K.J. (2017). Connecting particle fracture with electrochemical impedance in LiXMn2O4. J. Electrochem. Soc. *164*, A3709–A3717.

31. Mu, L., Lin, R., Xu, R., Han, L., Xia, S., Sokaras, D., Steiner, J.D., Weng, T.-C., Nordlund, D., Doeff, M.M., et al. (2018). Oxygen release induced chemomechanical breakdown of layered cathode materials. Nano Lett. *18*, 3241–3249.

32. Ko, D.-S., Park, J.-H., Park, S., Ham, Y.N., Ahn, S.J., Park, J.-H., Han, H.N., Lee, E., Jeon, W.S., and Jung, C. (2019). Microstructural visualization of compositional changes induced by transition metal dissolution in Ni-rich layered cathode materials by high-resolution particle analysis. Nano Energy *56*, 434–442.

33. Li, J., Li, W., You, Y., and Manthiram, A. (2018). Extending the Service Life of High-Ni Layered Oxides by Tuning the Electrode–Electrolyte Interphase. Adv. Energy Mater. *8*, 1801957.

34. Cha, J., Han, J.-G., Hwang, J., Cho, J., and Choi, N.-S. (2017). Mechanisms for electrochemical performance enhancement by the salt-type electrolyte additive, lithium difluoro (oxalato) borate, in high-voltage lithium-ion batteries. J. Power Sources *357*, 97–106.

35. Qian, Y., Niehoff, P., Börner, M., Grützke, M., Mönnighoff, X., Behrends, P., Nowak, S., Winter, M., and Schappacher, F.M. (2016). Influence of electrolyte additives on the cathode electrolyte interphase (CEI) formation on LiNi1/3Mn1/3Co1/3O2 in half cells with Li metal counter electrode. J. Power Sources *329*, 31–40.

36. Zhang, C., Liu, M., Pan, G., Liu, S., Liu, D., Chen, C., Su, J., Huang, T., and Yu, A. (2018). Enhanced Electrochemical Performance of LiNi0. 8Co0. 1Mn0. 1O2 Cathode for Lithium-Ion Batteries by Precursor Preoxidation. ACS Appl. Energy Mater. *1*, 4374–4384.

37. Ding, J., Lu, Z., Wu, M., Liu, C., Ji, H., and Yang, G. (2017). Preparation and performance characterization of AlF3 as interface stabilizer coated Li1. 24Ni0. 12Co0. 12Mn0. 56O2 cathode for lithium-ion batteries. Appl. Surf. Sci. *406*, 21–29.

38. Kim, J., Ma, H., Cha, H., Lee, H., Sung, J., Seo, M., Oh, P., Park, M., and Cho, J. (2018). A highly stabilized nickel-rich cathode material by nanoscale epitaxy control for high-energy lithium-ion batteries. Energy Environ. Sci. *11*, 1449–1459.

39. Hu, X., Qiang, W., and Huang, B. (2017). Surface layer design of cathode materials based on mechanical stability towards long cycle life for lithium secondary batteries. Energy Storage Materials *8*, 141–146.

40. Xiao, B., and Sun, X. (2018). Surface and subsurface reactions of lithium transition metal oxide cathode materials: an overview of the fundamental origins and remedying approaches. Adv. Energy Mater. *8*, 1802057.

41. Li, J., Li, Y., Guo, Y., Lv, J., Yi, W., and Ma, P. (2018). A facile method to enhance electrochemical performance of high-nickel cathode material Li (Ni 0.8 Co 0.1 Mn 0.1) O 2 via Ti doping. J. Mater. Sci. Mater. Electron. *29*, 10702–10708.

42. Huang, J., Liu, H., Zhou, N., An, K., Meng, Y.S., and Luo, J. (2017). Enhancing the Ion Transport in LiMn$_{1.5}$Ni$_{0.5}$O$_4$ by Altering the Particle Wulff Shape via Anisotropic Surface Segregation. ACS Appl. Mater. Interfaces *9*, 36745–36754.

43. Chen, L., Su, Y., Chen, S., Li, N., Bao, L., Li, W., Wang, Z., Wang, M., and Wu, F. (2014). Hierarchical Li1.2 Ni0.2 Mn0.6 O2 nanoplates with exposed 010 planes as high-performance cathode material for lithium-ion batteries. Adv. Mater. *26*, 6756–6760.

44. Xu, M., Fei, L., Zhang, W., Li, T., Lu, W., Zhang, N., Lai, Y., Zhang, Z., Fang, J., Zhang, K., et al. (2017). Tailoring anisotropic Li-ion transport tunnels on orthogonally arranged Li-rich layered oxide nanoplates toward high-performance Li-ion batteries. Nano Lett. *17*, 1670–1677.

45. Wei, G.Z., Lu, X., Ke, F.S., Huang, L., Li, J.T., Wang, Z.X., Zhou, Z.Y., and Sun, S.G. (2010). Crystal habit-tuned nanoplate material of Li [Li1/3-2x/3NixMn2/3-x/3]O$_2$ for high-rate performance lithium-ion batteries. Adv. Mater. *22*, 4364–4367.

46. Ernst, F., Kienzle, O., and Rühle, M. (1999). Structure and composition of grain boundaries in ceramics. J. Eur. Ceram. Soc. *19*, 665–673.

47. Yang, P., Zheng, J., Kuppan, S., Li, Q., Lv, D., Xiao, J., Chen, G., Zhang, J.-G., and Wang, C.-M. (2015). Phosphorus enrichment as a new composition in the solid electrolyte interphase of high-voltage cathodes and its effects on battery cycling. Chem. Mater. *27*, 7447–7451.

48. Lee, S.Y., Park, G.S., Jung, C., Ko, D.S., Park, S.Y., Kim, H.G., Hong, S.H., Zhu, Y., and Kim, M. (2019). Revisiting Primary Particles in Layered Lithium Transition-Metal Oxides and Their Impact on Structural Degradation. Adv. Sci. (Weinh.) *6*, 1800843.

49. Dawson, J.A., Canepa, P., Famprikis, T., Masquelier, C., and Islam, M.S. (2018). Atomic-scale influence of grain boundaries on Li-ion conduction in solid electrolytes for all-solid-state batteries. J. Am. Chem. Soc. *140*, 362–368.

50. Moriwake, H., Kuwabara, A., Fisher, C.A., Huang, R., Hitosugi, T., Ikuhara, Y.H., Oki, H., and Ikuhara, Y. (2013). First-principles calculations of lithium-ion migration at a coherent grain boundary in a cathode material, LiCoO(2). Adv. Mater. *25*, 618–622.

51. Tsai, P.-C., Wen, B., Wolfman, M., Choe, M.-J., Pan, M.S., Su, L., Thornton, K., Cabana, J., and Chiang, Y.-M. (2018). Single-particle measurements of electrochemical kinetics in NMC and NCA cathodes for Li-ion batteries. Energy Environ. Sci. *11*, 860–871.

52. Yan, P., Zheng, J., Zhang, J.-G., and Wang, C. (2017). Atomic resolution structural and chemical imaging revealing the sequential migration of Ni, Co, and Mn upon the battery cycling of layered cathode. Nano Lett. *17*, 3946–3951.

53. Wu, B., Bi, J., Liu, Q., Mu, D., Wang, L., Fu, J., and Wu, F. (2019). Role of current density in the degradation of LiNi0. 6Co0. 2Mn0. 2O2 cathode material. Electrochim. Acta *298*, 609–615.

54. Mussa, A.S., Klett, M., Behm, M., Lindbergh, G., and Lindström, R.W. (2017). Fast-charging to a partial state of charge in lithium-ion batteries: A comparative ageing study. Journal of Energy Storage *13*, 325–333.

55. Ruan, Y., Song, X., Fu, Y., Song, C., and Battaglia, V. (2018). Structural evolution and capacity degradation mechanism of LiNi0. 6Mn0. 2Co0. 2O2 cathode materials. J. Power Sources *400*, 539–548.

56. Schwartz, A.J., Kumar, M., Adams, B.L., and Field, D.P. (2009). Electron backscatter diffraction in materials science, *Volume 2* (Springer).

57. Humphreys, F. (2001). Review grain and subgrain characterisation by electron backscatter diffraction. J. Mater. Sci. *36*, 3833–3854.

58. Field, D.P. (1997). Recent advances in the application of orientation imaging. Ultramicroscopy *67*, 1–9.

59. Wright, S.I., and Nowell, M.M. (2006). EBSD image quality mapping. Microsc. Microanal. *12*, 72–84.

60. Bunge, H.-J. (2013). Texture analysis in materials science: mathematical methods (Elsevier).

61. Liu, Q. (1994). A simple method for determining orientation and misorientation of the cubic crystal specimen. J. Appl. Cryst. *27*, 755–761.

62. Ge, W., Wang, H., Xie, Z., Li, X., Qu, M., and Peng, G. (2017). Amorphous 0.035 Li2O-BPO4 coating for enhanced electrochemical performance of Li [Ni0. 5Co0. 2Mn0. 3] O2 cathode material. J. Alloys Compd. *693*, 606–614.

63. Zagorac, D., Müller, H., Ruehl, S., Zagorac, J., and Rehme, S. (2019). Recent developments in the Inorganic Crystal Structure Database: theoretical crystal structure data and related features. J. Appl. Cryst. *52*, 918–925.

64. Garcia, J.C., Bareño, J., Yan, J., Chen, G., Hauser, A., Croy, J.R., and Iddir, H. (2017). Surface structure, morphology, and stability of Li (Ni1/3Mn1/3Co1/3) O2 cathode material. J. Phys. Chem. C *121*, 8290–8299.

65. Sun, H., and Zhao, K. (2017). Electronic Structure and Comparative Properties of LiNi x Mn y Co z O2 Cathode Materials. J. Phys. Chem. C *121*, 6002–6010.

66. Zhu, G.-h., Mao, W.-m., and Yu, Y.-n. (2000). Calculation of misorientation distribution between recrystallized grains and deformed matrix. Scr. Mater. *42*, 37–42.

67. Persson, K., Sethuraman, V.A., Hardwick, L.J., Hinuma, Y., Meng, Y.S., Van Der Ven, A., Srinivasan, V., Kostecki, R., and Ceder, G. (2010). Lithium diffusion in graphitic carbon. J. Phys. Chem. Lett. *1*, 1176–1180.

68. Hielscher, R., Silbermann, C.B., and Schmidl, E. (2018). Denoising of Crystal Orientation Maps. J. Appl. Cryst. *52*, 984–996.

69. Hassold, G.N., Holm, E.A., and Miodownik, M.A. (2003). Accumulation of coincidence site lattice boundaries during grain growth. Mater. Sci. Technol. *19*, 683–687.

70. Hinz, D.C., and Szpunar, J.A. (1995). Modeling the effect of coincidence site lattice boundaries on grain growth textures. Phys. Rev. B Condens. Matter *52*, 9900–9909.

71. Randle, V. (2001). The coincidence site lattice and the 'sigma enigma'. Mater. Charact. *47*, 411–416.

72. Genieser, R., Ferrari, S., Loveridge, M., Beattie, S., Beanland, R., Amari, H., West, G., and Bhagat, R. (2018). Lithium ion batteries (NMC/graphite) cycling at 80° C: Different electrolytes and related degradation mechanism. J. Power Sources *373*, 172–183.

73. Tornheim, A., Sharifi-Asl, S., Garcia, J.C., Bareño, J., Iddir, H., Shahbazian-Yassar, R., and Zhang, Z. (2019). Effect of electrolyte composition on rock salt surface degradation in NMC cathodes during high-voltage potentiostatic holds. Nano Energy *55*, 216–225.

74. Zheng, S., Huang, R., Makimura, Y., Ukyo, Y., Fisher, C.A., Hirayama, T., and Ikuhara, Y. (2011). Microstructural changes in LiNi0. 8Co0. 15Al0. 05O2 positive electrode material during the first cycle. J. Electrochem. Soc. *158*, A357–A362.

75. Arganda-Carreras, I., Kaynig, V., Rueden, C., Eliceiri, K.W., Schindelin, J., Cardona, A., and Sebastian Seung, H. (2017). Trainable Weka Segmentation: a machine learning tool for microscopy pixel classification. Bioinformatics *33*, 2424–2426.